MicroRNA-155 negatively affects blood–brain barrier function during neuroinflammation

Miguel Alejandro Lopez-Ramirez,*,[1] Dongsheng Wu,* Gareth Pryce,[†] Julie E. Simpson,[‡] Arie Reijerkerk,[||],[2] Josh King-Robson,[†] Oliver Kay,[†] Helga E. de Vries,[||] Mark C. Hirst,* Basil Sharrack,[§] David Baker,[†] David Kingsley Male,* Gregory J. Michael,[†] and Ignacio Andres Romero*,[3]

*Department of Life, Health, and Chemical Sciences, Biomedical Research Network, The Open University, Milton Keynes, UK; [†]Center for Neuroscience and Trauma, Blizard Institute, Barts and The London School of Medicine and Dentistry, Queen Mary University of London, London, UK; [‡]Sheffield Institute for Translational Neuroscience and [§]Department of Neurology, Sheffield Teaching Hospitals National Health Service (NHS) Trust, University of Sheffield, Sheffield, UK; and [||]Blood–Brain Barrier Research Group, Molecular Cell Biology and Immunology, VU University Medical Center, Amsterdam, The Netherlands

ABSTRACT   Blood–brain barrier (BBB) dysfunction is a hallmark of neurological conditions such as multiple sclerosis (MS) and stroke. However, the molecular mechanisms underlying neurovascular dysfunction during BBB breakdown remain elusive. MicroRNAs (miRNAs) have recently emerged as key regulators of pathogenic responses, although their role in central nervous system (CNS) microvascular disorders is largely unknown. We have identified miR-155 as a critical miRNA in neuroinflammation at the BBB. miR-155 is expressed at the neurovascular unit of individuals with MS and of mice with experimental autoimmune encephalomyelitis (EAE). In mice, loss of miR-155 reduced CNS extravasation of systemic tracers, both in EAE and in an acute systemic inflammation model induced by lipopolysaccharide. In cultured human brain endothelium, miR-155 was strongly and rapidly upregulated by inflammatory cytokines. miR-155 up-regulation mimicked cytokine-induced alterations in junctional organization and permeability, whereas inhibition of endogenous miR-155 partially prevented a cytokine-induced increase in permeability. Furthermore, miR-155 modulated brain endothelial barrier function by targeting not only cell–cell complex molecules such as annexin-2 and claudin-1, but also focal adhesion components such as DOCK-1 and syntenin-1. We propose that brain endothelial miR-155 is a negative regulator of BBB function that may constitute a novel therapeutic target for CNS neuroinflammatory disorders.—Lopez-Ramirez, M. A., Wu, D., Pryce, G., Simpson, J. E., Reijerkerk, A., King-Robson, J., Kay, O., de Vries, H. E., Hirst, M. C., Sharrack, B., Baker D., Male, D. K., Michael, G. J., Romero, I. A. MicroRNA-155 negatively affects blood–brain barrier function during neuroinflammation. *FASEB J.* 28, 000–000 (2014). www.fasebj.org

IN NEURODEGENERATION, STROKE, and some neuroinflammatory diseases such as multiple sclerosis (MS), the permeability of the blood–brain barrier (BBB) increases, contributing to the onset and/or worsening of the disease. Although the mechanisms are not completely understood, they are thought to involve disassembly of the interendothelial junctional complex (IJC) and integrin focal adhesion (FA) complexes (1–3), probably as a result of altered expression of tight junction (TJ) proteins in response to proinflammatory cytokines, such as TNFα and IFNγ (4–6). *In vitro* these cytokines increase brain endothelial cell (BEC) permeability by modulation of gene expression at transcrip-

[1] Current address: Yale Cardiovascular Research Center, Section of Cardiovascular Medicine, Yale University School of Medicine. New Haven, CT 06511, USA.

[2] Current address: To-BBB Technologies BV, J. H. Oortweg, 2333 CH, Leiden, The Netherlands.

[3] Correspondence: Department of Life, Health, and Chemical Sciences, Biomedical Research Network, The Open University, Walton Hall, Milton Keynes, MK7 6AA, UK. E-mail: nacho.romero@open.ac.uk

tional and/or post-transcriptional levels (3, 5, 7). Recently, microRNAs (miRNAs) have emerged as important additional post-transcriptional regulators of gene expression that can silence target genes by translation inhibition, mRNA decay, or both (8). Indeed, miRNAs may constitute an important regulatory control of the brain endothelial response by fine tuning several of the cellular and molecular processes triggered by inflammatory mediators (7). Furthermore, deregulated miRNA levels have been demonstrated in several diseases, although their role in the pathogenesis of central nervous system (CNS) inflammatory disorders remains to be fully elucidated.

One of the best-characterized miRNAs is miR-155, which has pleiotropic functions in inflammation, autoimmunity, and cell plasticity (9–11). Thus far, miR-155 has been shown to induce a decrease in the expression levels of multiple identified transcripts, but the effect is modest, characteristic of fine-tuning regulation (12, 13). Moreover, endothelial miR-155 has been shown to regulate the expression of endothelial nitric oxide synthase following inflammatory stimulation (14). In the context of neuroinflammation, miR-155 has been shown to be one of the most highly elevated miRNAs in acute MS lesions (15). At a functional level, loss of miR-155 partially protects mice from the development of experimental allergic encephalomyelitis (EAE), a model of MS (10, 16). This finding correlates with its actions in promoting differentiation of TH17 cells (17), inhibiting TH2-type immune responses, and mediating activation of T cells, mononuclear phagocytes, and dendritic cells (10, 18, 19). However, the symptoms of EAE are related to increased BBB permeability, and it is equally possible that miR-155 acts directly in BECs to modulate BBB function.

In this study, we demonstrated altered levels of miR-155 at the neurovascular unit in MS brains and EAE spinal cords. $miR\text{-}155^{-/-}$ mice showed lower levels of BBB leakage in EAE and an acute model of systemic inflammation. Mechanistically, we found that miR-155 regulated human brain endothelial permeability by targeting molecules involved in cell-to-cell interactions, annexin-2 (ANXA-2) and claudin-1 (CLDN-1), and cell-to-extracellular matrix (ECM) interactions, dedicator of cytokinesis 1 (DOCK-1) and syntenin-1 (SDCBP). Our results demonstrated that brain endothelial miR-155 negatively regulates BBB function, thereby constituting a novel therapeutic target for MS and other neuroinflammatory conditions associated with BBB breakdown.

MATERIALS AND METHODS

Human and animal tissues

Human brain samples of patients with MS and control patients without neurological diseases were obtained from the UK Multiple Sclerosis Tissue Bank (Imperial College London, London, UK). Adult male and female (10–12 wk) Biozzi ABH mice were purchased from Harlan UK, Ltd.

(Bicester, UK), and $miR\text{-}155^{-/-}$ mice and $miR\text{-}155^{+/+}$ C57BL/6 mice were from Jackson Laboratory (Kent, UK). All procedures were approved after an ethics review, in accordance with the Animals (Scientific Procedures) Act 1986 of the UK government and the Animal Research: Reporting of *In Vivo* Experiments (ARRIVE) guidelines.

Induction of EAE

EAE was induced in Biozzi ABH mice with 1 mg freeze-dried mouse spinal cord homogenate in Freund's adjuvant supplemented with 60 mg *Mycobacterium tuberculosis* H37Ra and *Mycobacterium butyricum*. (20) In $miR\text{-}155^{-/-}$ or $miR\text{-}155^{+/+}$ C57BL/6 (B6.Cg-miR-155tm1.1Rsky/J) mice, EAE was induced with Hooke Kit (EK-2110) MOG35-55/CFA Emulsion PTX (Hooke Laboratories, Lawrence, MA, USA), according to the manufacturer's protocol. The animals were monitored daily to assess the development of relapsing–remitting paralysis and scored as follows: 0, normal; 1, limp tail; 2, impaired righting reflex; 3, hind limb paresis; and 4, complete hindlimb paralysis. The EAE status was based on paralytic clinical disease and weight loss/gain as follows: onset of signs (OS): clinical score 1, with weight loss sampled on d 15 postinduction; acute-phase paralysis (APP): clinical score 3.5–4, with weight loss by d 17; recovery: clinical score 3.5–1, with weight gain by d 20; remission one: clinical score 0.5, with weight gain by d 28 after induction; chronic: clinical score 3.5, with stable weight during remission from an episode 3 months after induction.

Laser capture microdissection (LCM) and isolation of microvessels

LCM was used to collect enriched brain endothelium RNA, by a rapid-staining protocol described in Supplemental Data (21).

Microvessels were isolated from the mouse spinal cords by a modified method (22). Briefly, EAE or normal ABH mice were perfused with Hanks' balanced salt solution containing 0.5% BSA, to rinse out the blood, and the spinal cords were flushed out. The spinal cords were digested with collagenase and dispase (1 mg/ml) at 37°C for 1 h, homogenized, and centrifuged with 25% BSA. The pellet of microvessels underwent a second digestion for 30 min and was purified by passage through a 70-μm mesh filter.

RNA extraction and microarray analysis

An immortalized human cerebral microvascular endothelial cell (hCMEC) line, hCMEC/D3, was cultured as described previously (3). Total RNA from 3 biological replicates were isolated with the miRNeasy Mini Kit (Qiagen, Crawley, UK), according to the manufacturer's protocol. Whole EAE and control spinal cords or isolated spinal cord microvessels were homogenized with TRIzol reagent, according to the manufacturer's protocol (Life Technologies, Paisley, UK). Total RNA of vessels *via* LCM was extracted with the RNAqueous-Micro Kit according to the manufacturer's instructions (Life Technologies). The quantity (1000 spectrophotometer; NanoDrop Technologies, Wilmington, DE, USA) and the quality (2100 bioanalyzer, RNA 6000 Pico LabChip; Agilent, Palo Alto, CA, USA) of the total RNA were analyzed. Detailed procedures and complete microarray data are available in the U.S. National Center for Biotechnology Information (Bethesda, MD, USA) Gene Expression Omnibus (GEO) under accession number GSE44694 (http://www.ncbi.nlm.nih.gov/geo).

Quantitative RT-PCR

The *Taq*Man MicroRNA Reverse Transcription Kit (Applied Biosystems, Warrington, UK) was used to synthesize single-stranded cDNA according to the manufacturer's protocol. Briefly, 2.5 ng of total RNA in the case of LCM material and 10 ng of total RNA in the case of spinal cords, isolated spinal microvessels, and cultured cells was used to synthesize single-stranded cDNA. Specific RT and PCR primers for hsa-miR-155 (000479–4427975), mmu-miR-155 (002571–4427975), hsa-miR-24 (000402–4427975), or RNU6B (001093–4440887), the internal control, were obtained from Life Technologies. *Taq*Man Universal PCR Master Mix (Life Technologies) was used to determine the relative levels of hsa-miRs, mmu-miR-155, and RNU6B. The reaction was then placed in a thermal cycler (DNA engine Opticon 2; Bio-Rad, Hemel Hempstead, UK) using an initial step at 95°C for 10 min for activation, followed by 40 cycles (15 s at 95°C and 60 s at 60°C), according to the manufacturer's protocol. The $2^{-\Delta\Delta CT}$ method was used for analysis of the data (23). Each control value for each experiment (unstimulated cells, whole spinal cords of control mice, microvessels from control human brains, and mouse spinal cords) was normalized to 1, and treatment or disease values are expressed relative to control values. SYBR Green real-time PCR (Qiagen) was used to determine the relative levels of murine *claudin-5*, (forward) CCTTCCTGGACCACAACATC and (reverse) CGCCAGCA-CAGATTCATACA; *Pecam-1*, (forward) GGACGATGCGATG-GTGTATAA and (reverse) GCATCACTGTGCATTTGTACTT; *Gfap*, (forward) CAGAGGAGTGGTATCGGTCTAA and (reverse) GATAGTCGTTAGCTTCGTGCTT; *Cd45*, (forward) CCCTTCTTCTGCCTCAAAGT and (reverse) CACCTGGAT-GATATGTGGTCTC, whereas *actin*, (forward) CTCCCTGGAGAA-GAGCTATGA, and (reverse) CCAAGAAGGAAGGCTGGAAA, mRNA levels were used as the internal control. The method $2^{-\Delta\Delta CT}$ was again used for analysis of the data (23). The results are expressed as relative abundance.

Immunohistochemistry and *in situ* hybridization (ISH)

EAE mice in acute-phase grade 4 (n=5) and control mice (n=5) were perfused with 4% paraformaldehyde (PFA) in 0.1 M phosphate buffer. After cryoprotection in sucrose and freezing, 15-μm sections of the lumbar spinal cords were cut onto SuperFrost Plus slides (VWR, Lutterworth, UK). The sections were first treated with 2 μg/ml proteinase K (Roche, Burgess Hill, UK) in 100 mM Tris HCl (pH 7.5) and 50 mM EDTA at 37°C for 10 min, then fixed again for 5 min in 4% PFA and dehydrated for 5 min in 70% ethanol. Sections were prehybridized in hybridization buffer consisting of 50% formamide; 5× saline sodium citrate (SSC; pH 7.0; 20× SSC contains 3 M NaCl and 0.3 M trisodium citrate; ref. 24); 100 μg/ml sheared salmon sperm DNA; and 0.1% Tween-20 at the miRNA probe hybridization temperature (52°C) for 30 min before the buffer was replaced with hybridization solution containing probe. Double digoxigenin–labeled miRcury LNA probe miR-155 oligonucleotide (5 nM; Exiqon, Vedbaek, Denmark) was hybridized with the sections overnight at 52°C. A similarly labeled LNA scrambled oligonucleotide (5 nM) with no complementary sequence in the mouse was used as the negative control in the same conditions. After hybridization, the sections were washed in a series of 5 min SSC washes at 55°C, consisting of 3 washes with 5× SSC, 3 washes with 1× SSC, and 3 washes with 0.2× SSC; and incubated for 15 min in a blocking buffer consisting of 0.5% blocking reagent (Roche) in TBST (100 mM Tris HCl, pH 7.5; 150 mM NaCl; and 0.1% Tween-20) before incubation overnight in rat anti-PECAM-1 (1:50; BD Biosciences, Oxford, UK), and sheep anti-digoxigenin antibody conjugated with alkaline phospha-tase (1:1000; Roche). Next, the sections were washed with TBST 4 times, 5 min each, before a wash in alkaline development buffer (100 mM Tris HCl, pH 9.5; 100 mM NaCl; 50 mM MgCl$_2$; and 0.1% Tween-20), and then incubated in NBT/BCIP (1%; Roche) and levamisole (0.5%; Vector Laboratories, Peterborough, UK) in alkaline development buffer at 30°C. After they were washed with TBST 4 times, 10 min each, the sections were incubated for 1 h with secondary goat anti-rat IgG conjugated to Alexa 488 (1:375; Life Technologies). Next, they were washed with TBST 4 times, 5 min each, before a wash in KTBST (50 mM Tris HCl, pH 7.5; 150 mM NaCl, 20 mM KCl, and 0.5% Tween-20) to reduce the background signal in the ISH. The cell nuclei were stained with DAPI Fluoromount-G (Southern Biotech, Birmingham, AL, USA). The slides were viewed with a fluorescence microscope and photographed in color with an Eclipse 80i fluorescence microscope (Nikon, Tokyo, Japan), a CX9000 digital camera (MBF Bioscience, Williston, VT, USA), and PictureFrame software (Optronics, Goleta, CA, USA).

Immunocytochemistry

hCMEC/D3 cells were grown to confluence on collagen-coated Lab-Tek multiwell chamber slides, and immunocytochemistry was performed (3). Briefly, hCMEC/D3 cells were fixed for 10 min at room temperature with 4% PFA in phosphate-buffered saline (PBS; pH 7.4) and then permeabilized with 0.5% Triton X-100 in PBS for 5 min. The slides were blocked with 0.5% BSA for 30 min and incubated with anti-ZO-1 (1:80; Life Technologies) and anti-vinculin (1:200; Sigma-Aldrich, Gillingham, UK). For talin immunostaining, the cells were fixed in methanol for 30 min at 4°C, followed by cold acetone (maintained at −20°C before use) for 1 min at room temperature and incubated with anti-talin (1:300; Sigma-Aldrich) antibody. Cells were washed with PBS and incubated for 1 h at room temperature with secondary goat anti-rabbit or -mouse Alexa Fluor 488 (Life Technologies). The slides were viewed with a BX61 fluorescence microscope for talin and vinculin (Olympus, Hatfield, UK) or a confocal microscope (Leica Microsystems, Mannheim, Germany) for ZO-1, and the images were captured with the Cell^P or Leica application suite (LAS) software (Leica Microsystems), respectively. For confocal microscopy, 15 images in Z stacks up to 2.5 μm in depth were acquired with a ×100 oil-immersion objective and projected onto 1 image.

Ectopic expression of miR-155 and siRNA transfections

hCMEC/D3 cells were seeded and grown to 70% confluence in EGM-2 MV medium before transfection, and the medium was then changed to EGM-2 MV (Lonza, Slough Wokingham, UK) supplemented with the following components obtained from the manufacturer: 0.1% (v/v) rhFGF, 0.1% (v/v) ascorbic acid, 0.04% (v/v) hydrocortisone, and 1.25% (v/v) FBS (hereafter referred to as transfection medium). To ectopically express miR-155 in hCMEC/D3 cells, we combined 30 nM of pre-miR-155 and the siPORT Amine transfection agent (Life Technologies) according to the manufacturer's instructions. Inhibition of endogenous miR-155 expression was performed by transfection with 60 nM of hsa-miR-155 miRID-IAN Hairpin Inhibitor (inhibitor miR-155; ThermoFisher Scientific, Epsom, UK). To silence human ANXA-2, DOCK-1, SDCBP, and CLDN-1, we used specific siGENOME SMART-pools (ThermoFisher Scientific). In both cases, inhibitor-miRs and siRNAs were combined with Lipofectamine 2000 (Life Technologies), according to the manufacturer's instructions. For all oligonucleotide, siPORT (pre-miRs) or lipo-

fectamine 2000 (inhibitor-miRs or siRNAs) were diluted in Opti-MEM I (Life Technologies), according to the manufacturer's protocols. The RNA oligonucleotide–lipofection agent complexes were then dispensed onto the hCMEC/D3 cells and incubated at 37°C for 6 h (Lipofectamine 2000) or 24 h (siPORT Amine). The transfection medium with oligonucleotide complexes was then replaced with fresh transfection medium for another 20 h (Lipofectamine 2000) or 2 h (siPORT Amine). The hCMEC/D3 cells were then maintained in EGM-2 MV culture medium without VEGF until the end of the experiment. Nontargeting, scrambled pre-miR, inhibitor-miR, or pooled siRNA was used as the transfection control.

Lentiviral transduction of 3′ untranslated region (UTR) reporter vectors and luciferase assay

The luciferase reporter lentiviral vector constructs containing the puromycin resistance gene and the Luciferase gene from the firefly *Photinus pyralis* with the 3′-UTR of *DOCK-1* (accession number NM_001380), *SDCBP* (accession number NM_005625), *ANXA-2* (accession number NM_005625), and *CLDN-1* (accession number NM_021101) were obtained from Applied Biological Materials, Inc. (Vancouver, BC, Canada).

To generate stable hCMEC/D3 cells, we used a multiplicity of infection of 3 for each of the 3′-UTR lentiviral constructs. Briefly, hCMEC/D3 cells were seeded to 40% confluence on 24-well plates. The cells were transduced with transduction medium containing 1×10^6 transducing U/ml of the lentiviral vector and 8 μg/ml of polybrene, all suspended in EGM-2 MV medium. After 12 h of transduction, the transduction medium was removed, and fresh EGM-2 MV medium was added. The hCMEC/D3 cells were grown to confluence and then apportioned into 6-well plates. Next, EGM-2 medium containing 2 μg/ml of puromycin was used to select the transduced cells.

Detection of luciferase was performed with the Steady-Glo Luciferase assay system according to the manufacturer's protocol (Promega, Madison, WI, USA). Cells were grown on collagen-coated, white, 96-well cell culture microplates (Greiner Bio-One, Monroe, NC, USA). Luciferase activity was detected with a plate reader (BMG, Ortenberg, Germany).

Western blot analysis

Cells were lysed by scraping them into a lysis solution containing 400 μl of RIPA buffer (25 mM Tris-HCl, pH 7.6; 150 mM NaCl; 1% Nonidet P-40; 1% sodium deoxycholate; and 0.1% SDS) and a cocktail of inhibitors (5 μg/ml aprotinin, leupeptin, and pepstatin and 1 mM sodium orthovanadate). After sonication, the amount of protein was determined with a Bio-Rad DC protein assay. The cell lysates were diluted in 1× Laemmli's buffer solution, at 95°C for 10 min. Total protein (25 μg/lane) was run on 12 and 10% SDS-polyacrylamide gels and transferred onto nitrocellulose membranes (Amersham, Little Chalfont, UK) by the wet-transfer system (Bio-Rad). The membranes were blocked with 5% nonfat milk/0.05% Tween-20 in PBS for 1 h and incubated in the presence of anti-DOCK-1 (1:200; Cell Signaling, Hitchin, UK), anti-SDCBP (1:100; AbD Serotec, Oxford, UK), anti-ANXA-2 (1:3000; BD Biosciences, Oxford, UK), and anti-CLDN-1 (1:125; Life Technologies) at room temperature overnight and then with a species-specific secondary anti-rabbit IgG (1:3000; Life Technologies) or anti-mouse IgG (1:14000; Pierce Biotechnology, Cheshire, UK) antibody conjugated to horseradish peroxidase for 1 h at room temperature. The immunoblots were then developed by enhanced chemiluminescence (ECL) detection (Amersham). As a con-trol for protein loading and transfer, the membranes were stripped for 40 min at 50°C and incubated with monoclonal antibody against actin (1:200; Sigma-Aldrich) and revealed as just described.

In vitro paracellular permeability assays

Cells were seeded onto collagen- and fibronectin-coated permeable polyester Transwell filter inserts (0.4 μm pore, 12 mm diameter; Corning Costar, High Wycombe, UK). The hCMEC/D3 cells were grown to 85% confluence, transfected as described earlier, and stimulated for 24 h with TNFα and IFNγ (1 ng/ml; R&D Systems, Abingdon, UK) or left untreated. The culture medium was then removed from the apical chamber, and 500 μl of transport buffer (2% FBS in DMEM without phenol red) containing 2 mg/ml 70 or 4 kDa FITC-dextran was added. The paracellular flux of tracer was then determined (3).

In vivo BBB permeability assays

On d 21 after induction of EAE, BBB permeability was determined by a published method, with modifications (25). Briefly, 70-kDa FITC-dextran (250 mg/kg) was injected intravenously, and 30 min later, the mice were transcardially perfused with 0.9% saline (400 ml/kg) and then with 4% PFA (800 ml/kg). Lumbar enlargement segments (L4–L5) were cross-sectioned at 20 μm thickness and mounted with DAPI-Fluoromount G. To determine the extravascular intensity of the FITC-dextran, images were obtained with fluorescence microscopy at ×40 (Zeiss, Cambridge, UK). The images were quantified with ImageJ software (U.S. National Institutes of Health, Bethesda, MD, USA) and normalized to fluorescence values in liver and to tissue area.

For the acute model of systemic inflammation, 12-wk-old male *miR-155*$^{-/-}$ or *miR-155*$^{+/+}$ C57BL/6 mice were injected with 2% Evans blue in PBS intraperitoneally at 80 mg/kg. At 18 h, lipopolysaccharide (LPS) from *Escherichia coli* O111:B4 (4 mg/kg; n=6) or PBS alone (n=4) was injected intraperitoneally (26). After 6 h, blood samples were collected by cardiac puncture, the mice were perfused with ice-cold 0.9% saline, and whole spinal cords were flushed out. Each spinal cord was homogenized in PBS and then mixed with 60% trichloroacetic acid and incubated on ice for 30 min. Supernatants were collected by centrifugation at 1000 *g* for 30 min. Absorbances of supernatants and plasma were read at λ 620 nm. Each absorbance value was then normalized to weight of the fresh spinal cords and to plasma concentrations of Evans blue.

Statistical analysis

Data are expressed as means ± SEM. For all experiments, the number of independent experiments (n) is indicated. The statistical analysis for the mRNA microarray was performed by using pairwise comparisons and false discovery rate. Statistical significance was set at $P < 0.01$, as determined by LIMMA software (WEHI Bioinformatics, Melbourne, VIC, Australia). For all other experiments, statistical significance was set at $P < 0.05$, as determined by paired, 2-tailed Student's *t* test (cultured cells) or by analysis of variance (ANOVA) with *post hoc* comparison and Tukey HSD correction (animal and human tissue) with SPSS software (SPSS, Chicago, IL, USA).

The FASEB Journal · www.fasebj.org

TABLE 1. *Demographic and clinical characteristics of MS and control brain samples*

Patient	Age/gender	*Post mortem*	MS type	Disease duration	Lesion activity	Cause of death
M1	54/F	22 h	Secondary progressive	Unknown	CAL/CL	Bronchopneumonia
M2	75/M	22 h	Secondary progressive	32 yr	CAL/CL	Pneumonia
M3	53/M	13 h	Secondary progressive	16 yr	CAL	Pneumonia
M4	34/F	12 h	Secondary progressive	Unknown	AL/CAL/CL	Pneumonia
M5	88/F	22 h	Primary progressive	30 yr	AL/CL	Bronchopneumonia
M6	72/F	8 h	Relapsing-remitting to secondary progressive	41 yr	AL/CAL/CL	Bronchopneumonia
C1	73/M	21 h	Control	NA	NA	Cardiogenic shock
C2	64/M	18 h	Control	NA	NA	Cardiac failure
C3	82/M	21 h	Control	NA	NA	Natural death
C4	35/M	22 h	Control	NA	NA	Tongue cancer
C5	84/M	5 h	Control	NA	NA	Bladder cancer
C6	82/M	21 h	Control	NA	NA	Rheumatoid arthritis

M, MS patient; C, control patient; CAL, chronic active lesions; AL, active lesions; CL, chronic lesions; NA, not applicable.

RESULTS

miR-155 is upregulated at the neurovascular unit of active MS lesions

We first investigated whether proinflammatory miR-155 (9) is altered at the level of the neurovascular unit in active MS lesions, using the LCM technique to isolate the microvasculature of white matter. We compared miR-155 levels in MS lesions with active, ongoing demyelination and inflammation with MS normal-appearing white matter (NAWM) and with levels in the white matter of nonneurological disease controls. Clinical information and the neuropathologic characterization of MS and control tissues used in this study are shown in **Table 1**. We observed that miR-155 at the neurovascular unit in MS lesions was significantly increased when compared to levels in MS-NAWM (**Fig. 1**) and in control NAWM (data not shown). These results suggest that increased levels of miR-155 at the neurovascular unit can be implicated in BBB dysfunction in MS.

miR-155 is differentially regulated during EAE and modulates paracellular permeability *in vivo*

To examine the temporal expression pattern of miR-155 in vivo, we initially induced EAE in Biozzi ABH mice, an animal model of MS that shows a predictable relapsing–remitting paralysis course associated with loss of BBB integrity at the spinal cord (20). We observed that the expression levels of miR-155 in whole spinal cords did not change at the onset of signs (EAE-OS, animals with limp tail; **Fig. 2A**). However, we observed that miR-155 levels were dramatically elevated in animals with APP (hind-limb paralysis) and during the recovery phase, reaching levels almost 15 times higher than in control animals. In addition, miR-155 increased levels were observed in the remission from the initial episode and chronic phases after remission from relapses, albeit to a lesser extent. To investigate whether miR-155 is upregulated in the CNS vasculature during

EAE, we extracted total RNA from isolated spinal cord microvessels. Quantitative RT-PCR (Fig. 2B) showed that expression of miR-155 in enriched spinal cord microvessels of EAE APP mice was 25 times higher than that of enriched microvessels in control mice. However, isolated spinal cord microvessels that contain high levels of markers for endothelial cells (*claudin-5* and *Pecam-1*) also showed minor amounts of astrocyte (*Gfap*) and leukocyte (*Cd45*) markers (Fig. 2C). To distinguish the endothelial miR-155 from other CNS resident cells or leukocytes, we performed ISH in combination with immunohistochemistry for the endothelial marker PECAM-1 in spinal cords of EAE-APP mice (Fig. 2D, E). We observed that miR-155 was upregulated in inflamed blood vessels and partially colocalized with endothelial PECAM-1 (Fig. 2F–H) and Glut-1 (Supplemental Fig. S1) expression, but not in the control littermates (Supplemental Fig. S1).
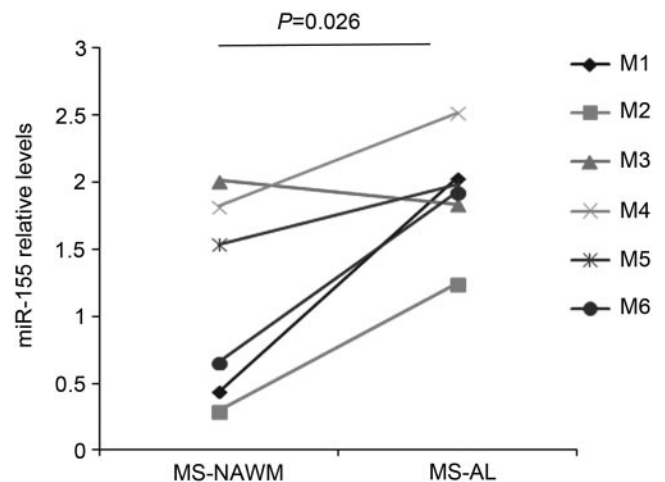

Figure 1. miR-155 is induced in active lesions of patients with MS. LCM was used to isolate cerebral blood vessels from active lesions of patients with MS (MS-AL) and MS-NAWM, and total RNA was then extracted. miR-155 expression levels were determined by quantitative RT-PCR. U6B small nuclear RNA was used as an internal standard. Patient numbers in the key to the graph refer to those in Table 1.
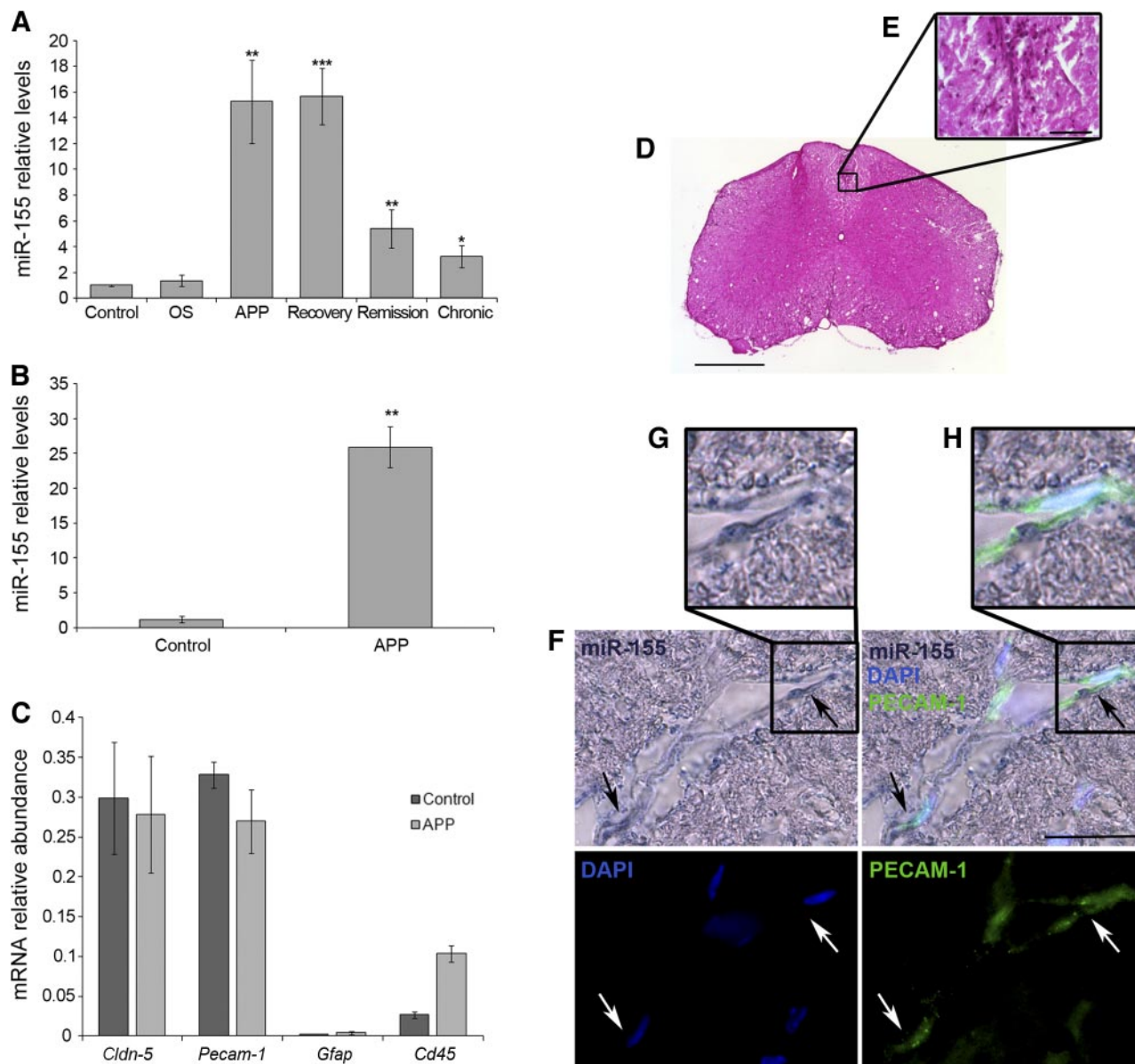
Figure 2. miR-155 is induced in spinal cords of EAE mice. *A*) EAE was induced in Biozzi ABH mice by using spinal cord homogenates, and total RNA from spinal cords at different clinical stages (OS, APP, recovery, remission, and chronic) were used to determine levels of miR-155 by quantitative RT-PCR. U6B small nuclear RNA was used as an internal standard. *P < 0.05, **P < 0.01, ***P < 0.001 *vs.* littermate controls (*n*=6). *B*) Total RNA from isolated spinal cord microvessels in EAE-APP mice and their control littermates were used to determine miR-155 levels by quantitative RT-PCR. Microvessels from the spinal cord of 3 mice were pooled and analyzed as 1 sample. Data are expressed as means ± SEM. **P < 0.01 *vs.* littermate controls (*n*=3). *C*) Total RNA in *B* was used to determine BEC (*Cldn-5* and *Pecam-1*), astrocyte (*Gfap*), and leukocyte (*Cd45*) markers by quantitative RT-PCR. *D*) Hematoxylin and eosin staining of a spinal cord from an EAE-APP mouse. Scale bar = 500 μm. *E*) Immune cell infiltration illustrated at higher magnification. Scale bar = 50 μm. *F–H*) ISH for miR-155 combined with immunohistochemistry to identify PECAM-1^{+} cells in the spinal cord of EAE-APP mice with a clinical score of 4. *F*) Bottom left: DAPI labels nuclei; white arrows show nucleus of BECs. Top left: expression of miR-155 (black arrow). *G*) Higher magnification. Bottom right: immunostaining of the endothelium-specific marker PECAM-1 (white arrows). Top right: merged image demonstrates colocalization of miR-155 and PECAM-1 (black arrows). *H*) Higher magnification. Scale bar = 25 μm.

These results led us to investigate whether the resistance of miR-155^{−/−} mice to EAE (**Fig. 3A** and refs. 10, 16) is in part associated with a decrease in vascular leakage in the region of inflammation. First, we observed that the *miR-155^{+/+}* and *miR-155^{−/−}* mice showed similar levels of leakage of 70-kDa FITC-dextran, indicating that BBB integrity was maintained in the *miR-155^{−/−}* mice (Fig. 3*B*, *C*). After induction of EAE, the soluble marker was found to be diffused through the spinal cord parenchyma and was in high abundance near the basolateral domain of inflamed blood vessels, indicative of BBB breakdown in the *miR-155^{+/+}* mice (Fig. 3*B*, *C*). In contrast to the *miR-155^{+/+}* EAE mice, the *miR-*
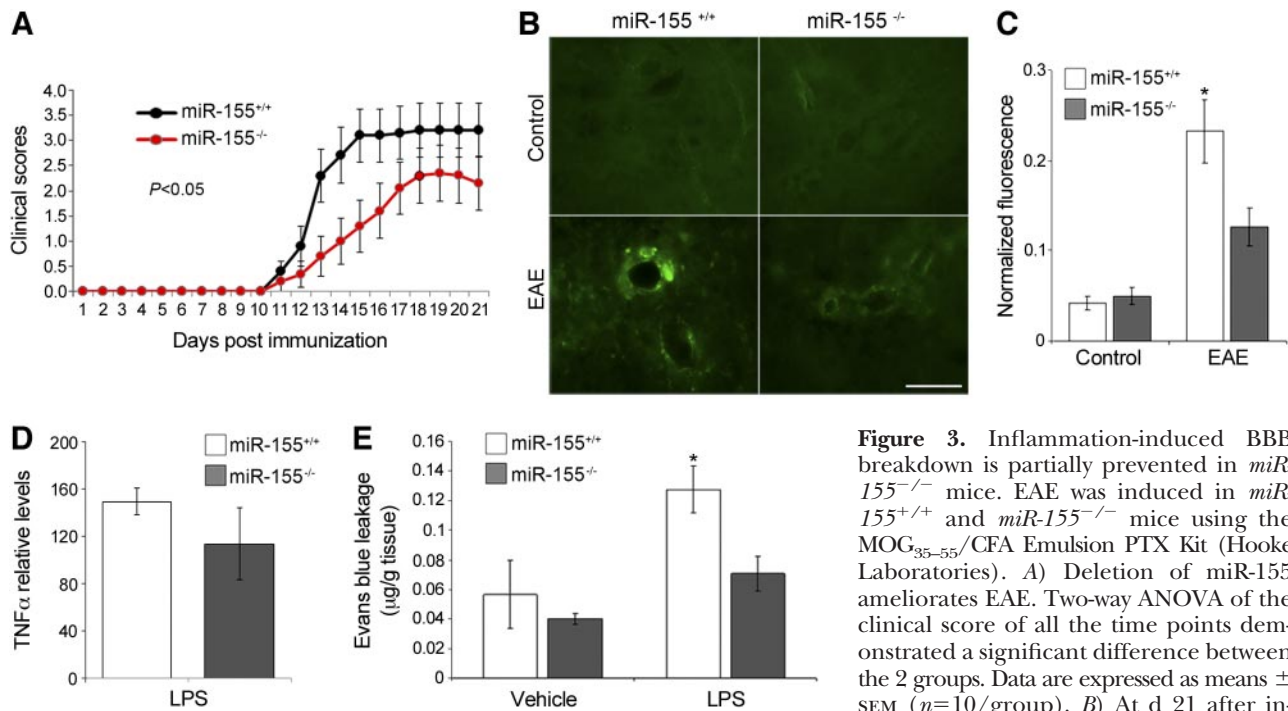
Figure 3. Inflammation-induced BBB breakdown is partially prevented in *miR-155$^{-/-}$* mice. EAE was induced in *miR-155$^{+/+}$* and *miR-155$^{-/-}$* mice using the MOG$_{35-55}$/CFA Emulsion PTX Kit (Hooke Laboratories). *A*) Deletion of miR-155 ameliorates EAE. Two-way ANOVA of the clinical score of all the time points demonstrated a significant difference between the 2 groups. Data are expressed as means ± SEM (*n*=10/group). *B*) At d 21 after induction, mice were injected intravenously with 70-kDa FITC-dextran (250 mg/kg), and lumbar spinal cords and livers were obtained after perfusion with fixative. Images of cross sections of spinal cords at the L4–L5 levels were analyzed to determine extravascular fluorescence intensity. Representative images show control nonimmunized *miR-155$^{+/+}$* and *miR-155$^{-/-}$* mice or immunized *miR155$^{+/+}$* and *miR-155$^{-/-}$* EAE mice. Scale bar = 25 μm. *C*) Quantification of extravascular intensity of 70-kDa FITC-dextran. For each mouse, the fluorescence intensity of spinal cord sections was normalized to that of liver sections from the same animal. Error bars = SEM (*n*=10). *P < 0.05 vs. all other groups; ANOVA with *post hoc* comparisons and Tukey HSD correction. *D*) Plasma levels of TNFα in WT and *miR-155$^{-/-}$* mice 6 h after intraperitoneal injection of LPS (4 mg/kg) assessed by ELISA. Values are fold change in LPS-treated wild-type (WT) and LPS-treated *miR-155$^{-/-}$* mice relative to that in PBS-treated WT (5.03±0.85 pg/ml) and PBS-treated *miR-155$^{-/-}$* (4.21±0.37 pg/ml) mice, respectively. Error bars = SEM (*n*=4 for PBS group, *n*=6 for LPS group). *E*) Quantification of efflux of Evans blue in the spinal cords of mice as in *D*. *P < 0.05 vs. all other groups; ANOVA with *post hoc* comparisons and Tukey HSD correction. Error bars = SEM (*n*=4, PBS group; *n*=6, LPS group).

155$^{-/-}$ EAE mice showed a 50% reduction in BBB leakage of the paracellular tracer (Fig. 3*B*, *C*). However, the reduced BBB leakage observed in the *miR-155$^{-/-}$* EAE mice may be due not only to a decrease in neurovascular dysfunction during neuroinflammation but also in part to a reduction in immune cell activation (9, 27).

To investigate the role of miR-155 in inflammation-induced neurovascular dysfunction with reduced leukocyte infiltration and/or leukocyte-triggered immune responses, such as TNFα secretion (Fig. 3*D*), we determined the BBB's permeability to Evans blue in an acute inflammation model induced by intraperitoneal injection of LPS. LPS administration induced a 2-fold increase of Evans blue leakage into spinal cords of the *miR-155$^{+/+}$* mice compared to that in the PBS-treated *miR-155$^{+/+}$* mice (Fig. 3*E*). By contrast, no increase in Evans blue extravasation was observed in the *miR-155$^{-/-}$* mouse spinal cords after LPS treatment when compared with that in the PBS-treated *miR-155$^{+/+}$* or *miR-155$^{-/-}$* mice (Fig. 3*E*). Overall, these results suggest a potential role of miR-155 expression at the neurovascular unit in the negative modulation of BBB function during neuroinflammation.

miR-155 modulates paracellular permeability of brain endothelium *in vitro*

We showed evidence of increased levels of miR-155 expressed at the neurovascular unit during neuroinflammation (Figs. 1 and 2*B*, *F*–*H* and Supplemental Fig. S1). However, our *in vivo* experiments did not unequivocally exclude indirect effects on neurovascular dysfunction by miR-155 expression in other CNS-resident cells, including astrocytes and pericytes. To better understand whether endothelial miR-155 directly mediates BBB dysfunction during neuroinflammation, we next investigated whether proinflammatory cytokines would alter levels of miR-155 in cultured human BECs. Indeed, miR-155 was upregulated in the hCMEC/D3 cell line by 2 cytokine treatments, including TNFα + IFNγ and TNFα + IL1β, but not by IFNγ + IL1β treatment (**Fig. 4*A***). We also observed a time- and dose-dependent increase in miR-155 expression levels in response to TNFα + IFNγ (Fig. 4*B*). We next investigated whether cytokine-induced up-regulation of miR-155 is associated with increased paracellular permeability in BECs. hCMEC/D3 cells were transfected with pre-miR-155 (Fig. 4*C*), and paracellular permea-
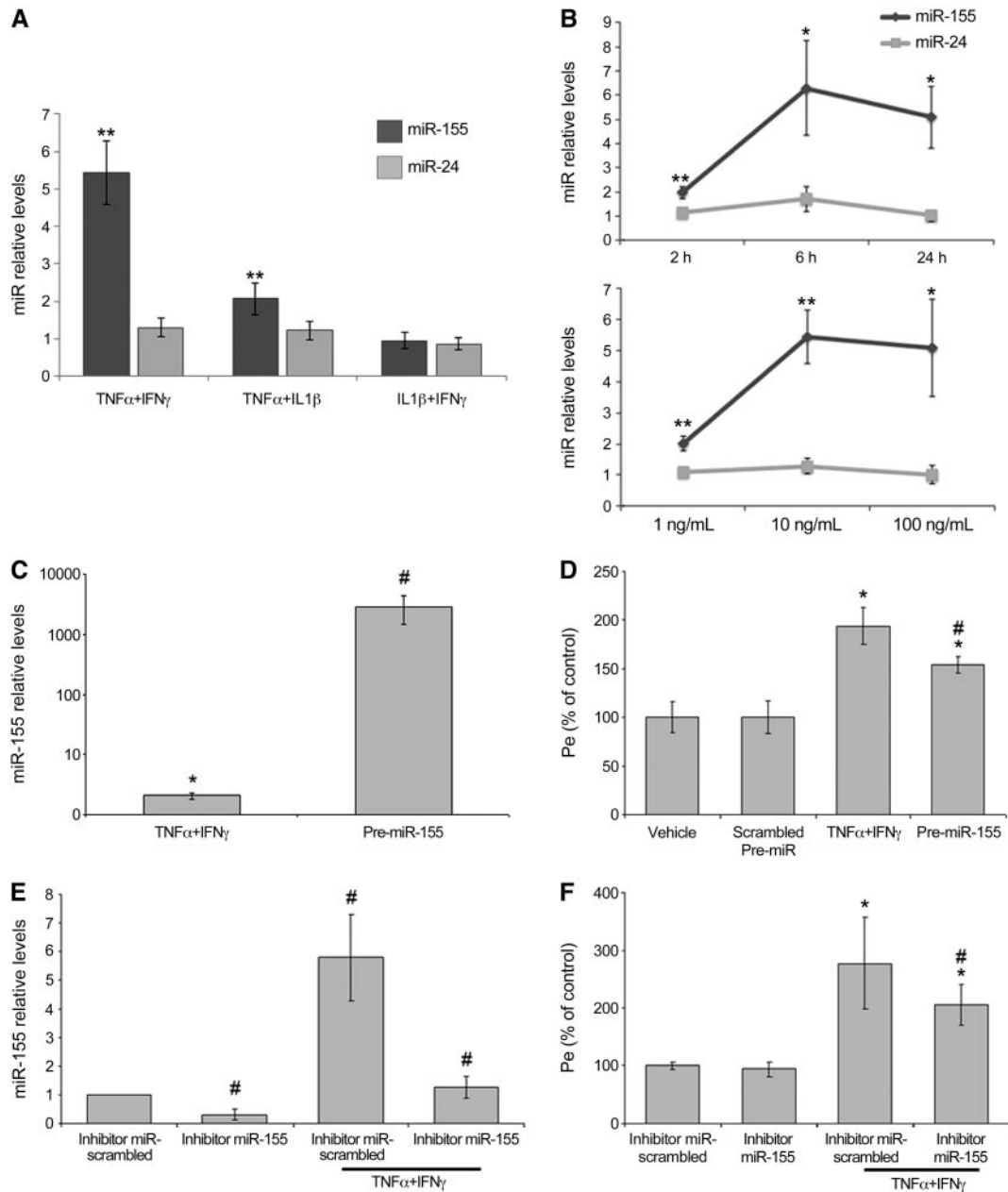
Figure 4. miR-155 contributes to cytokine-induced brain endothelial BBB breakdown *in vitro*. A) Total RNA was isolated from hCMEC/D3 cells treated with TNFα + IFNγ, TNFα + IL1β, or IL1β + IFNγ, to determine miR-155 levels by quantitative RT-PCR. miR-24 is an example of miRNA that did not change after cytokine treatment. U6B small nuclear RNA was used as an internal standard. Data are expressed as means ± SEM. **$P < 0.01$ *vs.* unstimulated cells ($n=3$). B) Confluent monolayers of hCMEC/D3 cells were stimulated with TNFα + IFNγ at 1, 10, and 100 ng/ml for 24 h or with TNFα + IFNγ (100 ng/ml) at 2, 6, and 24 h, to determine miR-155 levels by quantitative RT-PCR. Control values were normalized to 1; results are expressed as miRNA levels in TNFα + IFNγ-treated cells relative to those in unstimulated cells. Data are expressed as means ± SEM. *$P < 0.05$, **$P < 0.01$ *vs.* unstimulated cells ($n=3$). C) miR-155 expression levels in hCMEC/D3 cells treated with TNFα+IFNγ (1 ng/ml) or transfected with pre-miR-155 (30 nM) for 24 h. miRNA levels are expressed relative to those in control cells or in cells transfected with scrambled pre-miR. U6B small nuclear RNA was used as an internal standard. Data are expressed as means ± SEM ($n=3$). *$P < 0.05$ *vs.* vehicle-transfected cells; #$P < 0.05$ *vs.* scrambled pre-miR-transfected cells. D) Brain endothelial permeability coefficient (P_e) for 70-kDa FITC-dextran was measured in cells transfected with pre-miR-155 or stimulated with TNFα + IFNγ as in C. Data are expressed as means ± SEM ($n=3$). and *$P < 0.05$ *vs.* vehicle-transfected cells; #$P < 0.05$ *vs.* scrambled pre-miR-transfected cells. E) miR-155 levels were analyzed in hCMEC/D3 cells transfected with scrambled miR inhibitor (60 nM) or with miR-155 inhibitor (60 nM) in the presence or absence of TNFα + IFNγ (1 ng/ml) for 24 h. U6B RNA was used as an internal standard. Data are expressed as means ± SEM ($n=3$). #$P < 0.05$ *vs.* scrambled miR inhibitor-transfected cells. F) P_e for 70-kDa FITC-dextran was measured in hCMEC/D3 cells transfected with scrambled miR inhibitor or miR-155 inhibitor in the presence and absence of TNFα + IFNγ as in E. Data are expressed as means ± SEM ($n=3$). *$P < 0.05$ *vs.* basal scrambled miR inhibitor-transfected cells; #$P < 0.05$ *vs.* cytokine-treated scrambled miR inhibitor-transfected cells.

bility was assayed. First, we observed that low concentrations (1 ng/ml) of TNFα + IFNγ induced a 1.9-fold increase in the leakage of fluorescent dextrans across BEC monolayers when compared with that in the controls (Fig. 4D). Furthermore, the ectopic expression of miR-155 in hCMEC/D3 cells (Fig. 4C) induced a 1.5-fold increase in the leakage of both 4 (data not shown) and 70-kDa fluorescent dextrans, when compared with scrambled pre-miR-transfected cells (Fig. 4D). In contrast, hCMEC/D3 cells transfected with miR-155 inhibitor (Fig. 4E) partially reversed (by ~40%) the increase in paracellular permeability in the hCMEC/D3 cells challenged with 1 ng/ml of cytokines for 24 h (Fig. 4F). These results indicate that miR-155 contributes to the cytokine-induced disruption of the paracellular seal of the brain endothelium, which results in increased paracellular permeability to tracers *in vitro*.

Overexpression of miR-155 induces changes in the pattern of gene expression of hCMEC/D3 cells

To identify miR-155 target genes in BECs that might be implicated in BBB dysfunction relevant to human disease, we then used mRNA microarray analysis to analyze changes in mRNA expression of hCMEC/D3 cells that overexpress miR-155. We observed that 390 transcripts (of ~10,600 genes detected) were down-regulated by at least ~1.2-fold with a $P < 0.01$ significant change in overexpression of miR-155 (GEO accession number GSE44694). Using clueGO (28), we observed that the 3 most statistically significant biological processes identified were translation ($P<0.01$), FAs ($P<0.05$), and methionine metabolism ($P<0.05$; **Fig. 5A**). Another bioinformatic analytical source, DAVID (29), further identified IJC ($P<0.05$) as a significantly enriched functional category among the miR-155-down-regulated transcripts in hCMEC/D3 cells.

miR-155 induces reorganization of FAs and TJs in hCMEC/D3 cells

Since genes involved in FAs were markedly overrepresented in the set of genes down-regulated by the overexpression of miR-155 in hCMEC/D3 cells, we used immunocytochemical techniques to investigate whether FA organization is affected by modulation of miR-155 levels. Two structural components, vinculin and talin, showed a characteristic staining pattern of FAs, manifested by the presence of flat and elongated structures located centrally and near the cell periphery in hCMEC/D3 cells transfected with scrambled pre-miR (Fig. 5B, C). In addition, vinculin immunostaining was shown to be highly localized at the cell–cell junctions, as shown by the belt-like staining pattern on the cells' periphery (Fig. 5B).

After transfection with pre-miR-155, vinculin immunostaining located centrally did not appear to be affected in the hCMEC/D3 cells (Fig. 5B). However, we observed a substantial reduction in the staining of vinculin located at the cell–cell junctions (Fig. 5B). Ectopic expression of miR-155 also altered talin subcellular distribution located centrally and at cell borders (Fig. 5C). TNFα + IFNγ-treatment induced a change in the cell morphology, characterized by elongation of the cell shape accompanied by a reorganization of vinculin toward a more centrally localized and punctuate pattern (Fig. 5B). Inhibition of the cytokine-induced increase in miR-155 levels by miR-155 inhibitor partially rescued vinculin (Fig. 5B), but not talin (Fig. 5C), delocalization at the cell–cell junctions.

We also observed that ZO-1 showed a continuous intercellular junction pattern at the cell borders in hCMEC/D3 cells transfected with scrambled pre-miR and in nontransfected cells (Fig. 5D). By contrast, overexpressing miR-155 in BECs induced ZO-1 reorganization, characterized by disruption of its normal distribution from the cell–cell boundaries, similar to the effect of cytokines on junctional organization (Fig. 5D). Furthermore, cytokine-induced redistribution of ZO-1 (Fig. 5D) was partially prevented by miR-155 inhibitor (Fig. 5D). Altogether, these results led us to investigate the putative target genes involved in the miR-155-induced changes in FA and IJC organization that might contribute to alterations in the permeability of BECs.

Bioinformatic analysis and paracellular permeability assays identify 4 miR-155 putative targets associated with barrier dysfunction in hCMEC/D3 cells

Using TargetScan5.0 (8), we identified 63 putative target genes with a seed match for miR-155 that were down-regulated by overexpression of miR-155 at the mRNA level in hCMEC/D3 cells (**Fig. 6** and Supplemental Table S1). To further select candidate genes associated with the increased paracellular permeability induced by miR-155 in BECs, we used additional criteria by including only the genes associated with cell–cell junctions and/or the integrin adhesome (30–32) and those that were experimentally validated by 3′-UTR reporter assays in other cell types (12, 13, 33). Using this strategy, we identified 7 candidate genes, including 4 components of FAs, *DOCK-1, SDCBP, palladin* (*PALLD*), and *integrin αV* (*ITGAV*), and 3 molecules in IJCs, *ANXA-2, CLDN-1*, and *prion protein* (*PRNP*) (**Table 2**).

We then observed that reducing the expression of the FA components DOCK-1 and SDCBP induced a 1.4-fold increase in paracellular permeability when compared with that in the control (**Fig. 7A**). This effect was associated with delocalization of both ZO-1 and vinculin from the cell borders (Fig. 7B). Similarly, silencing CLDN-1 and ANXA-2 induced a 1.5-fold increase in paracellular permeability when compared with that in the controls (Fig. 7A). Silencing of CLDN-1 also induced disassembly of ZO-1 from the cell borders (data not shown). Silencing of the remaining 3 candidate genes, PALLD, ITGAV, and PRNP, did not induce
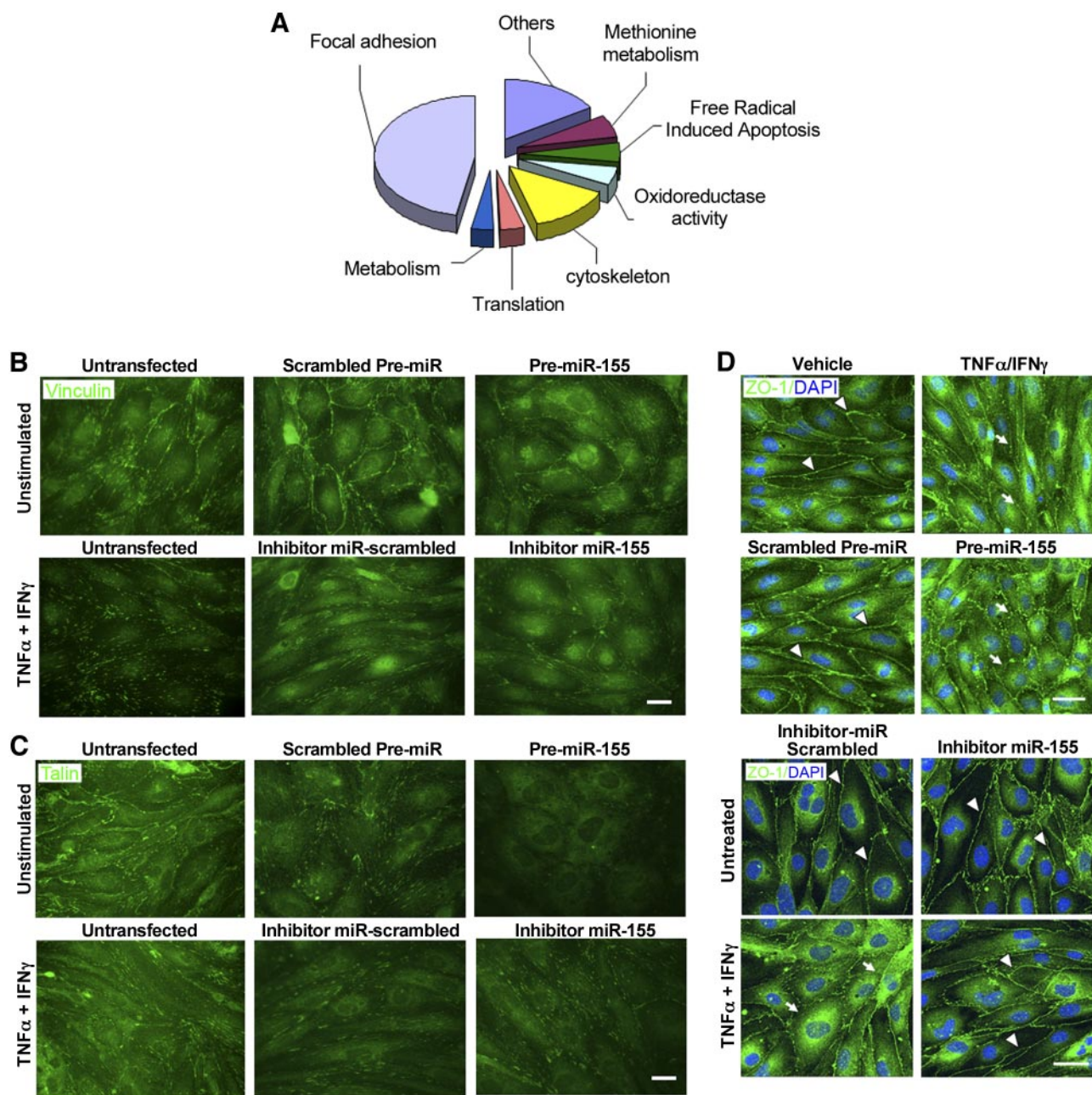
Figure 5. miR-155 induces changes in the pattern of gene expression of junctional molecules in hCMEC/D3 cells and alters their subcellular distribution. *A*) List of genes with down-regulated mRNA transcripts after ectopic expression of miR-155 in hCMEC/D3 cells, determined by microarray analysis, was used to create a pie visualization map with KEGG, Biocarta, and GO molecular functions by the ClueGO bioinformatic tool (28). Full data analysis of mRNA transcripts altered by overexpression of miR-155 in hCMEC/D3 cells can be accessed in GEO (accession number GSE44694). *B–D*) hCMEC/D3 cells were transfected with pre-miR-155 or miR-155 inhibitor before addition of TNFα + IFNγ (1 ng/ml) for 24 h. *B, C*) Vinculin (*B*) and talin (*C*) were used as FA markers and visualized by immunofluorescence. In nontransfected or scrambled pre-miR-transfected hCMEC/D3 cells, the vinculin and talin staining pattern was located centrally and at the cell borders. Overexpression of miR-155 induced the disappearance of vinculin primarily from the cell borders, whereas talin was delocalized, both from the cell borders and centrally. TNFα + IFNγ induced reorganization of both vinculin and talin in hCMEC/D3 cells, but only vinculin delocalization was partially prevented by miR-155 inhibitor. Images are representative of 3 separate experiments. Scale bar = 20 μm. *D*) Arrowheads show ZO-1 immunostaining in hCMEC/D3 cells characteristic of TJs discerned by continuous staining at the cell borders. Arrows show that miR-155 overexpression or TNFα + IFNγ stimulus for 24 h induced ZO-1 fragmentation from the cell–cell contacts compared with cells transfected with scrambled pre-miR or treated with vehicle. Knockdown of miR-155 using miR-155 inhibitor partially prevented cytokine-induced disassembly of ZO-1, as indicated by arrowheads (bottom right). Images are representative of 4 separate experiments. Scale bar = 25 μm.
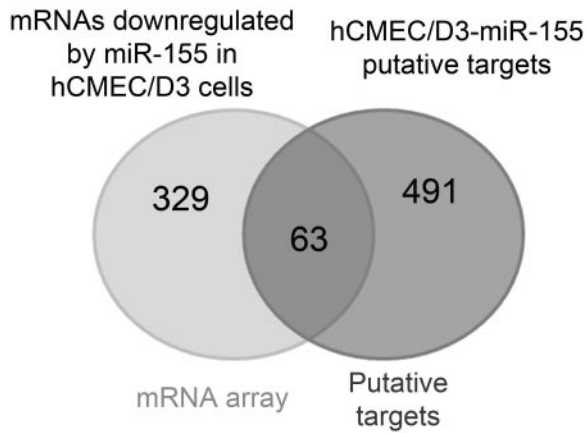
mRNAs downregulated by miR-155 in hCMEC/D3 cells

hCMEC/D3-miR-155 putative targets

329   63   491

mRNA array

Putative targets

Figure 6. miR-155 predicted targets in hCMEC/D3 cells. hCMEC/D3 cells were transfected with pre-miR-155 or with scrambled pre-miR as the control. RNA was extracted and analyzed using microarray profiling. hCMEC/D3 cells expressed ~10,600 genes of the ~24,000 genes tested. Shown are 2-way Venn diagram of genes down-regulated by ectopic expression of miR-155 and putative predicted targets for miR-155 expressed by hCMEC/D3 cells. Sixty-three genes were identified to have target sites for miR-155 and were down-regulated after ectopic expression of miR-155 in hCMEC/D3 cells. Table 2 shows the 7 candidate genes involved in miR-155-induced barrier breakdown in hCMEC/D3 cells.

an increase in the paracellular permeability of the hCMEC/D3 cells (data not shown).

We next validated the regulatory roles of miR-155 in FAs and IJCs by using the luciferase reporter assay. The results showed that miR-155 overexpression in the hCMEC/D3 cells decreased luciferase activity by ~30–40% in cells carrying the 3′-UTR of DOCK-1, SDCBP, ANXA-2, or CLDN-1, when compared with the scrambled pre-miR controls (Fig. 7C). These results were further supported by a decrease in the protein levels of DOCK-1 (~65%), SDCBP (~50%), ANXA-2 (~30%), and CLDN-1 (~50%) in hCMEC/D3 cells overexpressing miR-155, as evidenced by immunoblot analysis (Fig. 7D, E). These results demonstrate that 4 target genes for miR-155, including 2 components of FAs, DOCK-1 and SDCBP, and 2 components of IJCs, ANXA-2 and CLDN-1, modulate brain endothelial permeability and potentially mediate, at least partially, miR-155-induced BBB breakdown during inflammation.

DISCUSSION

We propose that miR-155 acts as a novel negative regulator of BBB function during neuroinflammation by modulating BEC cell-to-cell and cell-to-matrix interactions, thereby contributing to the pathogenesis of CNS neuroinflammatory disorders such as MS. The general consensus is that miR-155 is a proinflammatory miRNA (9) and that it may participate in the harmonization of cell activation during inflammatory processes in mammals. Consistent with this proposal, a recent study has shown that miR-155 is highly expressed in active inflammatory MS plaques where astrocytes were identified as one of the potential cellular sources of this miRNA (15). Our current results further suggest that miR-155 is highly expressed at the neurovascular unit in MS active lesions and is differentially upregulated in mouse whole spinal cords at different stages of EAE. Indeed, we used an animal model that shows a reproducible and predictable relapsing–remitting EAE (20). During EAE-OS there is an infiltration of leukocytes and BBB leakage (20) without any significant changes in miR-155 levels in whole spinal cords, suggesting that the cellular source of miR-155 at this stage is low and/or difficult to detect if the increase in miR-155 is restricted to a few affected areas of the neurovascular unit. However, miR-155 levels are rapidly upregulated during paralysis in the initial APP at a time when maximum cell infiltration is occurring around the vasculature (20). Furthermore, in this EAE model, the recovery occurs when the animals begin to gain weight and clinical scores subside (20). This is accompanied by a gradual recovery of BBB function and reduction of cellular infiltration of the CNS (20), but we did not observe a decrease in the proinflammatory miR-155 levels. This result suggests that the proinflammatory cytokine profile at this stage is still high. It is tempting to speculate that activation mechanisms that initiate the

TABLE 2. *Candidate genes involved in miR-155-induced BBB breakdown in hCMEC/D3 cells*

	HeLa cells							
TargetScan	Guo *et al.* (11)	Selbach *et al.* (11)	B cells; Xu *et al.* (33)	DR	Gene symbol	Gene name	FA	JC
×			×	×	*CLDN-1*	Claudin 1		×
×	×			×	*ANXA-2*	Annexin A2		×
×	×			×	*PRNP*	Prion protein (p27–30)		×
×	×	×	×	×	*SDCBP*	Syntenin 1	×	
×	×			×	*DOCK-1*	Dedicator of cytokenesis 1	×	
×	×			×	*PALLD*	Palladin	×	
×	×			×	*ITGAV*	Integrin αV	×	

Criteria for selection: *1*) genes down-regulated at the mRNA level by ectopic expression of miR-155 (the full data analysis of mRNA transcripts altered by overexpression of miR-155 in hCMEC/D3 cells can be accessed in GEO with accession number GSE44694); *2*) genes with function related to cell–cell or cell–matrix adhesion; and *3*) miR-155 predicted targets as identified by databases (Targetscan) and/or experimentally validated by 3′ UTR-reporter assays in other cell types (see refs. 12, 13, 33). DR, down-regulated in hCMEC/D3 cells; FA, focal adhesion; JC, junctional complex.
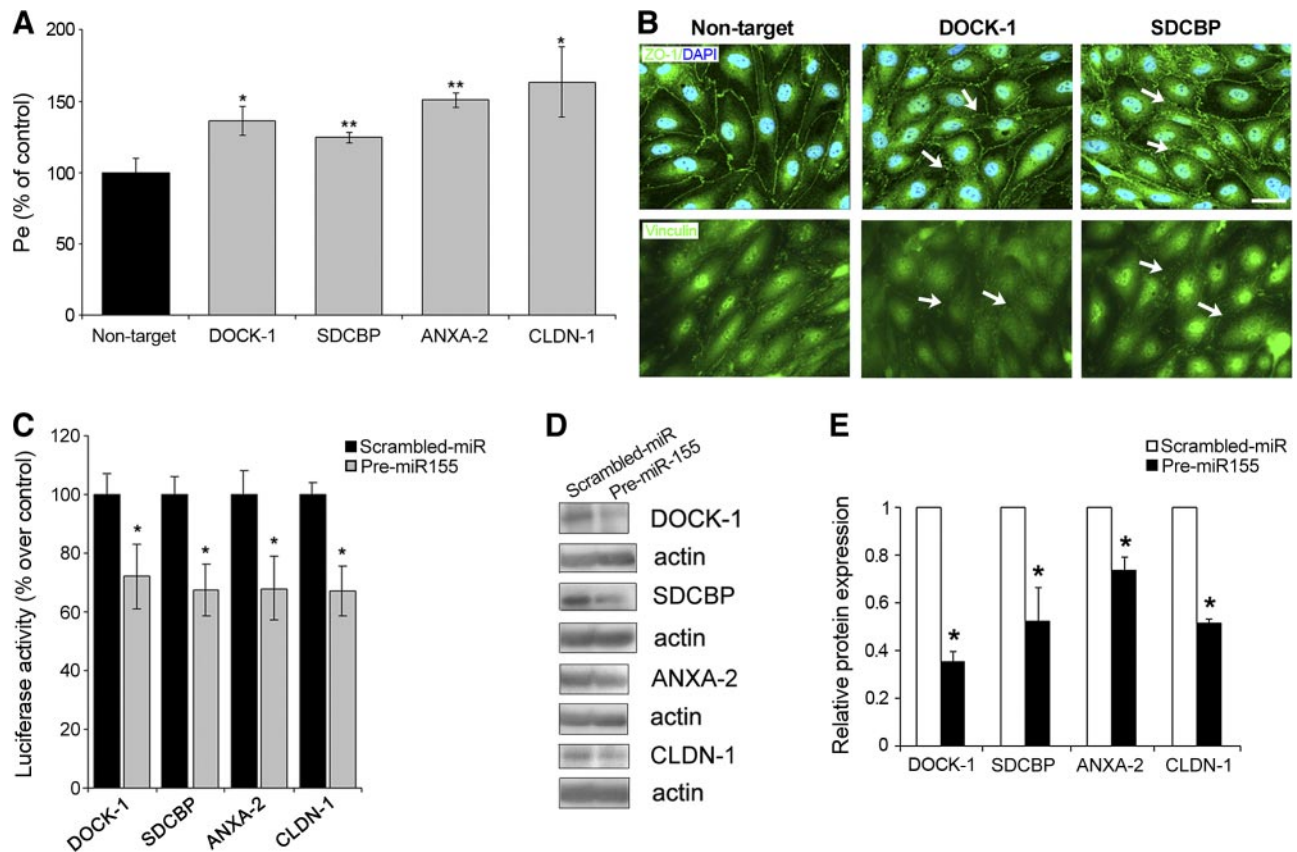
Figure 7. miR-155 silences genes associated with cell–cell and cell–matrix junctions, leading to increased paracellular permeability in hCMEC/D3 cells. *A*) Silencing of *DOCK-1*, *SDCBP*, *ANXA-2*, or *CLDN-1* using specific siRNAs induced an increase in hCMEC/D3 cell paracellular permeability to FITC-dextran. Error bars = SEM (*n*=3–4). *$P < 0.05$, **$P < 0.01$ *vs.* nontarget siRNA negative control. *B*) Silencing of *DOCK-1* or *SDCBP* using specific siRNAs induced delocalization of ZO-1 and vinculin from the cell periphery, denoted by arrows. Images are representative of 3 separate experiments. Scale bar = 20 µm. *C*) Cells were transiently transfected with pre-miR-155 or scrambled pre-miR in hCMEC/D3 cells stably expressing luciferase constructs with the 3′-UTR of the indicated genes. Ectopic expression of miR-155 reduces luciferase activity for each construct. Data are expressed as means ± SEM (*n*=3). *$P < 0.05$ *vs.* scrambled pre-miR-transfected cells. *D*) DOCK-1, SDCBP, ANXA-2, and CLDN-1 protein levels were determined by Western blot analysis in hCMEC/D3 cells transfected with scrambled pre-miR or pre-miR-155. The same blots were reprobed with anti-actin antibody as indicated for each gene. *E*) Protein expression levels in *D* were quantified using ImageJ software and presented as the means ± SEM (*n*=3). *$P < 0.05$ *vs.* scrambled pre-miR-transfected cells.

resolution of the inflammatory response during the recovery phase also, by an unknown molecular mechanism, desensitize the neurovascular unit to the effects of miR-155 before any decrease in miR-155 levels is observed. This desensitizing effect may also occur in the first remission phase when inflammatory lesions resolve and BBB dysfunction is minimal but miR-155 levels are still elevated (20). Another cellular source of miR-155 in EAE spinal cords may be activated leukocytes, since mononuclear cells, including T lymphocytes with increased miR-155 levels, infiltrate the CNS parenchyma in EAE (10, 16). However, increased miR-155 levels at the neurovascular unit were observed in isolated microvessels of EAE spinal cords. We also observed by ISH that, during neuroinflammation, miR-155 appeared to be expressed in the microvasculature as well as in large blood vessels, including venules.

Previous studies have shown that BBB breakdown is a fundamental event during the course of MS and that the magnitude of the neurovascular dysfunction in EAE is associated with the neurological severity of the disease (34). Furthermore, mice deficient in the *bic/miR-155* gene showed partial resistance to the development of EAE in this and previous studies (10, 16) and, in this study, we showed that loss of miR-155 plays a protective role against BBB leakage in the region of inflammation. In addition, using LPS as an acute model of systemic inflammation with reduced leukocyte infiltration and circulating TNFα response, we observed that loss of miR-155 attenuates the increase in BBB permeability. However, these *in vivo* experiments are not conducive to unequivocally excluding the effect of miR-155 on other CNS-resident cells, astrocytes and pericytes, during neurovascular inflammation. To test the hypothesis that brain endothelial miR-155 is involved in BBB dysfunction, we examined the effects of miR-155 on brain endothelial barrier functions in cell culture. Brain endothelial miR-155 was upregulated by proinflammatory cytokines in a time- and dose-dependent manner, an effect that coincides with cytokine-medi-

ated brain endothelial barrier permeability (3). Moreover, in our study, the ectopic expression of miR-155 mimicked the cytokine-induced increase in permeability, whereas knockdown of endogenous miR-155 partially prevented cytokine-induced barrier disruption in BECs, indicating an active role for endothelial miR-155 in inflammation-induced BBB breakdown. Hence, brain endothelial miR-155 appears to be a proinflammatory miRNA, but it is induced by inflammation and/or infection at early times after stimuli, suggesting that it contributes to the early stages of inflammation at the neurovascular unit.

The mechanism by which miR-155 may exacerbate the breakdown of the BBB appears to involve 2 different cellular pathways. First, miR-155 may be an important "control node" for the expression of IJC molecules in brain endothelium, thereby directly affecting the organization of cell–cell junctions. Consistent with our results, Kong *et al.* (35) reported that miR-155 induced delocalization of ZO-1 from the cell–cell contacts in tumorigenic epithelial cells. In this study, we found that miR-155 may modulate BEC permeability and TJ organization by directly targeting the components of IJCs: CLDN-1 and ANXA-2. CLDN-1, a target for miR-155, has an important barrier function, at least in epithelial cells (36), although its expression by BECs *in vivo* is controversial (37). Recently, it has been shown that ectopic expression of CLDN-1 in C57BL/6 mice prevents BBB leakiness in EAE animals, compared with that in littermate controls (32). Furthermore, loss of CLDN-1 at the BBB has also been associated with barrier dysfunction in glioblastoma multiforme (38) and hepatitis C infection (39). In addition, ANXA-2, another miR-155 target, has been shown to regulate endothelial cell morphology and junctional integrity *via* its association with VE-cadherin (31). However, little is known about the contribution of ANXA-2 to strengthening the BEC barrier. In our study, silencing of ANXA-2 expression had significant consequences for BEC barrier function *in vitro*. Hence, miR-155 direct targeting of at least 2 components of CNS IJCs may lead to increased BBB permeability.

A second cellular pathway modulated by endothelial miR-155 involves FA organization, which may also lead to increased BBB permeability after application of a cytokine stimulus. We observed that miR-155 affects the distribution of vinculin and talin in BECs, suggesting alterations in the cellular attachment to their matrix substrate. Vinculin is a cytoskeleton-associated protein that plays an important role in FA assembly and strength (40). Talin, another FA molecule, directly interacts with the cytoplasmic tail of β-integrins, inducing their activation (41). Indeed, β1-integrin-mediated adhesion of BECs to the surrounding ECM has recently been shown to be critical for stabilizing claudin-5 in TJs and for BBB integrity (42). In our study, we observed that miR-155 has the capacity to directly target FA components in BECs and that down-regulation of at least some of these components may lead to increased BEC permeability. For instance, DOCK-1 forms part of

focal contacts and participates in the downstream integrin signal transduction pathway by forming complexes with the engulfment and cell motility (ELMO) protein (43). It is possible that the DOCK-1-ELMO complex, a guanine nucleotide exchange factor, regulates endothelial permeability by modulating the activity of Rho-family GTPases such as Rac-1, although this does not exclude the possibility that FA disassembly directly leads to increased BEC permeability (44). Indeed, another FA molecule that we found to be regulated by miR-155 in cultured BEC is SDCBP, an adaptor and scaffold protein that contains PDZ (postsynaptic density protein-95, postsynaptic discs large, and zona occludens-1) motifs. Initially, SDCBP was shown to interact with syndecans, which are heparan sulfate proteoglycans that assist cell adhesion and promote attraction and concentration of growth factors at the cell surface (45). It has also been shown that knockdown of SDCBP prevents fibronectin-induced formation of integrin-β1/FAK/c-Src complex, which may play an important role in the downstream focal contact signaling pathway (46). Therefore, it appears that not only structural FA proteins are important for stabilizing TJs and the brain endothelial barrier but also FA adaptor and signaling proteins. Whereas in other cell types such as fibroblasts (47), miR-155 may promote migration by silencing genes implicated in modulating cell-to-matrix attachment, endothelial miR-155 may indirectly contribute to increased BBB permeability *via* targeting FA components.

In summary, we propose that miR-155 modulates key features of the brain endothelial barrier during inflammation and may play an important role during the pathogenesis of CNS inflammatory disorders that affect the BBB. In addition, endothelial miR-155 may act as an effector of inflammatory mediators associated with promotion of inflammation and subsequent barrier breakdown. In this study, we demonstrated the possibility that miR-155 contributes to BBB breakdown during neuroinflammation by altering the phenotype and function of neurovascular endothelium, in particular components of cell-to-cell and cell-to-matrix adhesion pathways, thereby revealing potential therapeutic targets for the amelioration of CNS inflammatory disorders. FJ

REFERENCES

1. Lopez-Ramirez, M. A., Male, D. K., Wang, C., Sharrack, B., Wu, D., and Romero, I. A. (2013) Cytokine-induced changes in the gene expression profile of a human cerebral microvascular endothelial cell-line, hCMEC/D3. *Fluids Barriers CNS* **10,** 27

2. Schlegel, N., and Waschke, J. (2009) Impaired integrin-mediated adhesion contributes to reduced barrier properties in VASP-deficient microvascular endothelium. *J. Cell. Physiol.* **220,** 357–366

3. Lopez-Ramirez, M. A., Fischer, R., Torres-Badillo, C. C., Davies, H. A., Logan, K., Pfizenmaier, K., Male, D. K., Sharrack, B., and Romero, I. A. (2012) Role of caspases in cytokine-induced barrier breakdown in human brain endothelial cells. *J. Immunol.* **189,** 3130–3139

4. Mankertz, J., Tavalali, S., Schmitz, H., Mankertz, A., Riecken, E., Fromm, M., and Schulzke, J. (2000) Expression from the human occludin promoter is affected by tumor necrosis factor alpha and interferon gamma. *J. Cell Sci.* **113,** 2085–2090

5. Forster, C., Burek, M., Romero, I. A., Weksler, B., Couraud, P. O., and Drenckhahn, D. (2008) Differential effects of hydrocortisone and TNFalpha on tight junction proteins in an in vitro model of the human blood-brain barrier. *J. Physiol.* **586,** 1937–1949

6. Murakami, T., Felinski, E. A., and Antonetti, D. A. (2009) Occludin phosphorylation and ubiquitination regulate tight junction trafficking and vascular endothelial growth factor-induced permeability. *J. Biol. Chem.* **284,** 21036–21046

7. Reijerkerk, A., Lopez-Ramirez, M. A., van het Hof, B., Drexhage, J. A., Kamphuis, W. W., Kooij, G., Vos, J. B., van der Pouw Kraan, T. C., van Zonneveld, A. J., Horrevoets, A. J., Prat, A., Romero, I. A., and de Vries, H. E. (2013) microRNAs regulate human brain endothelial cell barrier function in inflammation: implications for multiple sclerosis. *J. Neurosci.* **17,** 6857–6863

8. Friedman, R. C., Farh, K. K.-H., Burge, C. B., and Bartel, D. P. (2009) Most mammalian mRNAs are conserved targets of microRNAs. *Genome Res.* **19,** 92–105

9. Baltimore, D., Boldin, M., O'Connell, R., Rao, D., and Taganov, K. (2008) MicroRNAs: new regulators of immune cell development and function. *Nat. Immunol.* **9,** 839–845

10. O'Connell, R. M., Kahn, D., Gibson, W. S., Round, J. L., Scholz, R. L., Chaudhuri, A. A., Kahn, M. E., Rao, D. S., and Baltimore, D. (2010) MicroRNA-155 promotes autoimmune inflammation by enhancing inflammatory T cell development. *Immunity* **33,** 607–619

11. Kong, W., Yang, H., He, L., Zhao, J.-J., Coppola, D., Dalton, W. S., and Cheng, J. Q. (2008) MicroRNA-155 Is regulated by the transforming growth factor β/Smad pathway and contributes to epithelial cell plasticity by targeting RhoA. *Mol. Cell. Biol.* **28,** 6773–6784

12. Guo, H., Ingolia, N. T., Weissman, J. S., and Bartel, D. P. (2010) Mammalian microRNAs predominantly act to decrease target mRNA levels. *Nature* **466,** 835–840

13. Selbach, M., Schwanhausser, B., Thierfelder, N., Fang, Z., Khanin, R., and Rajewsky, N. (2008) Widespread changes in protein synthesis induced by microRNAs. *Nature* **455,** 58–63

14. Sun, H. X., Zeng, D. Y., Li, R. T., Pang, R. P., Yang, H., Hu, Y. L., Zhang, Q., Jiang, Y., Huang, L. Y., Tang, Y. B., Yan, G. J., and Zhou, J. G. (2012) Essential role of microRNA-155 in regulating endothelium-dependent vasorelaxation by targeting endothelial nitric oxide synthase. *Hypertension* **60,** 1407–1414

15. Junker, A., Krumbholz, M., Eisele, S., Mohan, H., Augstein, F., Bittner, R., Lassmann, H., Wekerle, H., Hohlfeld, R., and Meinl, E. (2009) MicroRNA profiling of multiple sclerosis lesions identifies modulators of the regulatory protein CD47. *Brain* **132,** 3342–3352

16. Murugaiyan, G., Beynon, V., Mittal, A., Joller, N., and Weiner, H. L. (2011) Silencing microRNA-155 ameliorates experimental autoimmune encephalomyelitis. *J. Immunol.* **187,** 2213–2221

17. Yao, R., Ma, Y. L., Liang, W., Li, H. H., Ma, Z. J., Yu, X., and Liao, Y. H. (2012) MicroRNA-155 modulates Treg and Th17 cells differentiation and Th17 cell function by targeting SOCS1. *PloS One* **7,** e46082

18. O'Connell, R. M., Taganov, K. D., Boldin, M. P., Cheng, G., and Baltimore, D. (2007) MicroRNA-155 is induced during the macrophage inflammatory response. *Proc. Natl. Acad. Sci. U.S.A.* **104,** 1604–1609

19. Dunand-Sauthier, I., Santiago-Raber, M. L., Capponi, L., Vejnar, C. E., Schaad, O., Irla, M., Seguin-Estevez, Q., Descombes, P., Zdobnov, E. M., Acha-Orbea, H., and Reith, W. (2011) Silencing of c-Fos expression by microRNA-155 is critical for dendritic cell maturation and function. *Blood* **117,** 4490–4500

20. Al-Izki, S., Pryce, G., Jackson, S. J., Giovannoni, G., and Baker, D. (2012) Immunosuppression with FTY720 is insufficient to prevent secondary progressive neurodegeneration in experimental autoimmune encephalomyelitis. *Mult. Scler.* **17,** 939–948

21. Simpson, J. E., Ince, P. G., Shaw, P. J., Heath, P. R., Raman, R., Garwood, C. J., Gelsthorpe, C., Baxter, L., Forster, G., Matthews, F. E., Brayne, C., and Wharton, S. B. (2011) Microarray analysis of the astrocyte transcriptome in the aging brain: relationship to Alzheimer's pathology and APOE genotype. *Neurobiol. Aging* **32,** 1795–1807

22. Abbott, N. J., Hughes, C. C., Revest, P. A., and Greenwood, J. (1992) Development and characterisation of a rat brain capillary endothelial culture: towards an in vitro blood-brain barrier. *J Cell Sci.* **103,** 23–37

23. Livak, K. J., and Schmittgen, T. D. (2001) Analysis of relative gene expression data using real-time quantitative PCR and the 2-ΔΔCT method. *Methods* **25,** 402–408

24. Obernosterer, G., Martinez, J., and Alenius, M. (2007) Locked nucleic acid-based in situ detection of microRNAs in mouse tissue sections. *Nat. Protoc.* **2,** 1508–1514

25. Hoffmann, A., Bredno, J., Wendland, M., Derugin, N., Ohara, P., and Wintermark, M. (2011) High and low molecular weight fluorescein isothiocyanate (FITC)-dextrans to assess blood-brain barrier disruption: technical considerations. *Transl. Stroke. Res.* **2,** 106–111

26. Manaenko, A., Chen, H., Kammer, J., Zhang, J. H., and Tang, J. (2011) Comparison Evans Blue injection routes: intravenous versus intraperitoneal, for measurement of blood–brain barrier in a mice hemorrhage model. *J. Neurosci. Methods* **195,** 206–210

27. Rodriguez, A., Vigorito, E., Clare, S., Warren, M. V., Couttet, P., Soond, D. R., van Dongen, S., Grocock, R. J., Das, P. P., Miska, E. A., Vetrie, D., Okkenhaug, K., Enright, A. J., Dougan, G., Turner, M., and Bradley, A. (2007) Requirement of bic/microRNA-155 for normal immune function. *Science* **316,** 608–611

28. Bindea, G., Mlecnik, B., Hackl, H., Charoentong, P., Tosolini, M., Kirilovsky, A., Fridman, W.-H., Pagès, F., Trajanoski, Z., and Galon, J. (2009) ClueGO: a Cytoscape plug-in to decipher functionally grouped gene ontology and pathway annotation networks. *Bioinformatics* **25,** 1091–1093

29. Huang, D. W., Sherman, B. T., and Lempicki, R. A. (2008) Systematic and integrative analysis of large gene lists using DAVID bioinformatics resources. *Nat. Protoc.* **4,** 44–57

30. Zaidel-Bar, R., Itzkovitz, S., Ma'ayan, A., Iyengar, R., and Geiger, B. (2007) Functional atlas of the integrin adhesome. *Nat. Cell Biol.* **9,** 858–867

31. Su, S.-C., Maxwell, S. A., and Bayless, K. J. (2010) Annexin 2 regulates endothelial morphogenesis by controlling AKT activation and junctional integrity. *J. Biol. Chem.* **285,** 40624–40634

32. Pfeiffer, F., Schafer, J., Lyck, R., Makrides, V., Brunner, S., Schaeren-Wiemers, N., Deutsch, U., and Engelhardt, B. (2011) Claudin-1 induced sealing of blood-brain barrier tight junctions ameliorates chronic experimental autoimmune encephalomyelitis. *Acta Neuropathol.* **122,** 601–614

33. Xu, G., Fewell, C., Taylor, C., Deng, N., Hedges, D., Wang, X., Zhang, K., Lacey, M., Zhang, H., Yin, Q., Cameron, J., Lin, Z., Zhu, D., and Flemington, E. K. (2010) Transcriptome and targetome analysis in MIR155 expressing cells using RNA-seq. *RNA* **16,** 1610–1622

34. Fabis, M. J., Phares, T. W., Kean, R. B., Koprowski, H., and Hooper, D. C. (2008) Blood-brain barrier changes and cell invasion differ between therapeutic immune clearance of neurotrophic virus and CNS autoimmunity. *Proc. Natl. Acad. Sci. U.S.A.* **105,** 15511–15516

35. Kong, W., He, L., Coppola, M., Guo, J., Esposito, N. N., Coppola, D., and Cheng, J. Q. (2008) MicroRNA-155 regulates cell survival, growth, and chemosensitivity by targeting FOXO3a in breast cancer. *J. Biol. Chem.* **285,** 17869–17879

36. Inai, T., Kobayashi, J., and Shibata, Y. (1999) Claudin-1 contributes to the epithelial barrier function in MDCK cells. *Eur. J. Cell Biol.* **78,** 849–855

37. Wolburg, H., Wolburg-Buchholz, K., Kraus, J., Rascher-Eggstein, G., Liebner, S., Hamm, S., Duffner, F., Grote, E.-H., Risau, W., and Engelhardt, B. (2003) Localization of claudin-3 in tight junctions of the blood-brain barrier is selectively lost during

experimental autoimmune encephalomyelitis and human glio-blastoma multiforme. *Acta Neuropathol.* **105,** 586–592

38. Liebner, S., Fischmann, A., Rascher, G., Duffner, F., Grote, E., Kalbacher, H., and Wolburg, H. (2000) Claudin-1 and claudin-5 expression and tight junction morphology are altered in blood vessels of human glioblastoma multiforme. *Acta Neuropathol.* **100,** 323–331

39. Fletcher, N. F., Wilson, G. K., Murray, J., Hu, K., Lewis, A., Reynolds, G. M., Stamataki, Z., Meredith, L. W., Rowe, I. A., Luo, G., Lopez-Ramirez, M. A., Baumert, T. F., Weksler, B., Couraud, P. O., Kim, K. S., Romero, I. A., Jopling, C., Morgello, S., Balfe, P., and McKeating, J. A. (2012) Hepatitis C virus infects the endothelial cells of the blood-brain barrier. *Gastroenterology* **142,** 634–643

40. Ziegler, W. H., Gingras, A. R., Critchley, D. R., and Emsley, J. (2008) Integrin connections to the cytoskeleton through talin and vinculin. *Biochem. Soc. Trans.* **36,** 235–239

41. Nayal, A., Webb, D. J., and Horwitz, A. F. (2004) Talin: an emerging focal point of adhesion dynamics. *Curr. Opin. Cell Biol.* **16,** 94–98

42. Osada, T., Gu, Y. H., Kanazawa, M., Tsubota, Y., Hawkins, B. T., Spatz, M., Milner, R., and Del Zoppo, G. J. (2011) Interendo-thelial claudin-5 expression depends on cerebral endothelial cell-matrix adhesion by beta(1)-integrins. *J. Cereb. Blood Flow Metab.* **31,** 1972–1985

43. Komander, D., Patel, M., Laurin, M. l., Fradet, N., Pelletier, A., Barford, D., and Cote, J. F. (2008) An alpha-helical extension of the ELMO1 Pleckstrin homology domain mediates direct inter-action to DOCK180 and is critical in Rac signaling. *Mol. Biol. Cell* **19,** 4837–4851

44. Epting, D., Wendik, B., Bennewitz, K., Dietz, C. T., Driever, W., and Kroll, J. (2010) The Rac1 regulator ELMO1 controls vascular morphogenesis in zebrafish. *Circ. Res.* **107,** 45–55

45. Beekman, J. M., and Coffer, P. J. (2008) The ins and outs of syntenin, a multifunctional intracellular adaptor protein. *J. Cell Sci.* **121,** 1349–1355

46. Hwangbo, C., Kim, J., Lee, J. J., and Lee, J. H. (2010) Activation of the integrin effector kinase focal adhesion kinase in cancer cells is regulated by crosstalk between protein kinase Calpha and the PDZ adapter protein mda-9/syntenin. *Cancer Res.* **70,** 1645–1655

47. Pottier, N., Maurin, T., Chevalier, B., Puissagur, M.-P., Lebrig-and, K., Robbe-Sermesant, K., Bertero, T., Lino Cardenas, C. L., Courcot, E., Rios, G., Fourre, S., Lo-Guidice, J.-M., Marcet, B., Cardinaud, B., Barbry, P., and Mari, B. (2009) Identification of keratinocyte growth factor as a target of microRNA-155 in lung fibroblasts: implication in epithelial-mesenchymal interactions. *PloS One* **4,** e6718